Science
AAAS

Supplementary Materials for

Cryo-EM structure of a mitochondrial calcium uniporter

Jiho Yoo[1,†], Mengyu Wu[2,†], Ying Yin[1], Mark A. Herzik Jr[2], Gabriel C. Lander[2,*], Seok-Yong Lee[1,*]

*Correspondence to:
S.-Y. Lee
email: seok-yong.lee@duke.edu
telephone: 919-684-1005

G.C. Lander
email: glander@scripps.edu
telephone: 858-784-8793

†These authors contributed equally.

This PDF file includes:

Materials and Methods
Figs. S1 to S10
Tables S1
References

Materials and Methods

Protein expression and purification

After a screen of over 50 MCU orthologues, *Neurospora crassa* mitochondrial calcium uniporter (MCU_{NC}) showed optimal biochemical stability. The N-terminal mitochondrial targeting sequence (MTS, residues 1-45) was predicted by Mitoprot (https://ihg.gsf.de/ihg/mitoprot.html) (*31*). A bacterial codon-optimized gene encoding MCU_{NC} without MTS (residues 46-493, Uniprot: Q7S4I4) was synthesized (BioBasic Inc). The MCU_{NC} gene was subcloned into pET26(b) vector in frame with a C-terminal hexa-histidine tag. To prevent the partial proteolysis at the N-terminal region of MCU_{NC}, a point mutation Tyr232Ala was introduced using the Quikchange mutagenesis kit (Agilent). This mutation was identified by analysis of the proteolysis pattern of MCU_{NC} on SDS-PAGE and by systematic mutagenesis of potential proteolysis sites. For protein expression, MCU_{NC} (Tyr232Ala) construct was transformed into C41(DE3) *E. coli* strain. The cells were grown in Terrific Broth medium at 37 °C until an OD_{600} of 0.8 and were induced with 0.4 mM IPTG. Protein was expressed at 20 °C for 16 h. The culture was harvested by centrifugation at 5000 rpm for 10 min. Cells were resuspended in lysis buffer (50 mM Tris-HCl pH 8.0, 150 mM NaCl, 5 μg ml^{-1} leupeptin, 5 μg ml^{-1} pepstatin, 5 μg ml^{-1} aprotinin, 1 mM phenylmethylsulfonyl fluoride and DNaseI) and were lysed by microfluidizer (Microfluidics). To solubilize the protein, 40 mM n-dodecyl-β-D-maltopyranoside (DDM, Anatrace) and 0.1 mg ml^{-1} cardiolipin (Avanti Polar Lipid) were added to the cell lysate, followed by stirring at 4 °C for 2 h. Insoluble fraction was removed by centrifugation at 15000 rpm for 30 min at 4 °C. The supernatant was incubated with TALON cobalt resin (Clontech) in the presence of 15 mM imidazole with gentle agitation for 30 min at 4 °C. The resin was transferred into a gravity column and washed with 10 column volumes of wash buffer (20 mM Tris-HCl pH 8.0, 150 mM NaCl, 1 mM DDM, 15 mM imidazole, 0.1 mg ml^{-1} cardiolipin). Protein was eluted with 5 column volumes of elution buffer (20 mM Tris-HCl pH 8.0, 150 mM NaCl, 1 mM DDM, 200 mM imidazole, 0.1 mg ml^{-1} cardiolipin). The protein was further purified by size-exclusion chromatography (SEC) using a Superose 6 10/300 GL column (GE Healthcare) equilibrated with SEC buffer A (20 mM HEPES pH 8.0, 150 mM NaCl, 1 mM DDM, 0.1 mg ml^{-1} cardiolipin, 2 mM DTT, 2 mM $CaCl_2$). The peak fractions were analyzed by SDS-PAGE and collected for cryo-EM and cross-linking studies. The sample was prepared under two different Ca^{2+} conditions. One was prepared at a low concentration of Ca^{2+}, wherein 2 mM Ca^{2+} was present during initial stages of purification but was removed at the final size-exclusion chromatography step prior to EM grid preparation. The other sample was prepared at a high Ca^{2+} concentration, wherein 2 mM Ca^{2+} was present throughout purification and EM grid preparation.

Chemical cross-linking

The oligomeric state of MCU_{NC} was characterized by chemical cross-linking using an amine-group specific and water-soluble cross-linker, BS3 (Sulfo-DSS, Thermofisher). BS3 was first dissolved in water to a concentration of 50 mM and further diluted to 5 mM with SEC buffer A. 0.25 mg ml^{-1} protein purified in DDM was mixed with BS3 at a working of concentration of 0 μM, 25 μM, 75 μM, 250 μM, and 500 μM respectively and incubated at room temperature for 30 min. Reactions were quenched by 50 mM Tris-HCl pH 8.0 and analyzed on 4-15% SDS-PAGE.

For cryo-EM study, the flexible N-terminal domains (NTDs) of MCU_{NC} were stabilized by BS3 using optimized conditions. In a 2.5-ml reaction, protein purified in DDM was diluted with SEC buffer A to 0.25 mg ml^{-1} and mixed with BS3 at a working concentration of 250 μM (see preparation above). The reaction was incubated at room temperature for 30 min and was quenched

by 20 mM Tris-HCl pH 8.0. The reaction product was subsequently reconstituted into lipid nanodiscs (see below).

Nanodisc reconstitution

BS3 cross-linked MCU_{NC} was concentrated to 2 mg ml^{-1} and reconstituted into lipid nanodiscs following published protocol (*32*) with modifications. In brief, BS3 cross-linked MCU_{NC}, MSP2N2, and lipid (1-palmitoyl-2-oleoyl-*sn*-glycero-3-phosphocholine (POPC):1-palmitoyl-2-oleoyl-*sn*-glycero-3-phosphoethanolamine (POPE):1-palmitoyl-2-oleoyl-*sn*-glycero-3-phospho-(1′-*rac*-glycerol) (POPG)=3:1:1, w/w) were mixed at a molar ratio of 1:4:200 and incubated at 4 °C for 1 h. To remove detergent, Bio-Beads SM2 (Bio-Rad) were added to a concentration of 100 mg ml^{-1} followed by gentle agitation at 4 °C for 2 h. The Bio-Beads were replaced with a fresh batch of equal amount and were incubated at 4 °C for 16 h with gentle agitation. After the Bio-beads were removed, the supernatant was further purified on a Superose 6 10/300 GL column equilibrated with SEC buffer B (20mM Tris-HCl pH 8.0, 150 mM NaCl, 2 mM $CaCl_2$). Protein from the peak fractions was subjected to cryo-EM study.

Amphipol reconstitution

As described above, MCU_{NC} was purified by size-exclusion chromatography in SEC buffer C (20 mM Tris-HCl pH 8.0, 150 mM NaCl, 1 mM DDM, 0.1 mg ml^{-1} cardiolipin, 2 mM DTT). The protein peak (without BS3 cross-linking) was concentrated to 1-1.5 mg ml^{-1} with a volume of 1-1.5 ml. Protein was mixed with Amphipol PMAL-C8 (Avanti polar lipid) at 1:10 (w/w) ratio and incubated overnight at 4 °C with gentle agitation. Detergent was removed by 25 mg ml^{-1} Bio-Beads SM-2 (Bio-Rad) at 4 °C for 2 h. The reconstituted protein was further purified on a Superose 6 10/300 GL column equilibrated with SEC buffer D (20 mM Tris-HCl pH 8.0, 150mM NaCl). Protein from the peak fractions was subjected to cryo-EM study.

EM sample preparation

For negatively-stained MCU_{NC}, 3 µl of WT or Y232A protein (0.04 mg/ml) in amphipol was applied to freshly glow-discharged 400 Cu-Rh Maxtaform grids (Electron Microscopy Services) that had been coated with a thin layer of carbon. The sample was incubated on the grid for 3 s and wicked away using Whatman #1 filter paper. 3 µl of ~1% (w/v) uranyl formate solution was applied directly to the grid and excess stain was wicked away immediately. The procedure was repeated once more with a 30s incubation time, followed by blotting to dryness.

For cryo-EM, 3 µL of native MCU_{NC} in amphipol (1.5 mg/ml) or cross-linked MCU_{NC} in nanodiscs (3.2 mg/ml) was applied to freshly plasma cleaned UltrAuFoil® R1.2/1.3 300-mesh grids (Quantifoil) and manually blotted (*33*) using a custom-built manual plunger in a cold room (≥95% relative humidity, 4°C). Sample was blotted for ~4 seconds with Whatman No.1 filter paper immediately prior to plunge freezing in liquid ethane cooled by liquid nitrogen.

EM data acquisition and image processing

All cryo-EM data were acquired using the Leginon automated data-acquisition program (*34*). All image pre-processing (frame alignment, CTF estimation, particle picking) were performed in real-time using the Appion image-processing pipeline (*35*) during data collection.

Images of negatively stained WT and Y232A MCU_{NC} were collected on a Tecnai F20 (FEI) transmission electron microscope (TEM) operating at 200 keV. Images were collected at a nominal magnification of 62,000x on a FEI Eagle CCD (4k) camera, corresponding to a pixel size of

1.79 Å/pixel. All micrographs were collected with an electron dose of ~42 e-/Å^2 using a defocus range from −0.8 to −2 μm. A total of 101 micrographs were collected of the WT sample and 142 micrographs were collected of the Y232A sample. CTF estimation was performed using CTFFIND4 (*36*). Difference of Gaussians (DoG) picker (*37*) was used to automatically pick particles from the micrographs, yielding a stack of 73,065 particles and 50,155 particles from the WT and Y232A samples, respectively, that were binned 2 × 2 (3.57 Å/pixel, 80-pixel box size) and subjected to reference-free 2D classification using multivariate statistical analysis (MSA) and multi-reference alignment (MRA)(*38*).

Images of frozen hydrated MCU_{NC} were collected on a Talos Arctica (Thermo Fisher) TEM operating at 200 keV (*39*). Movies were collected using a K2 Summit direct electron detector (Gatan) in counting mode at a nominal magnification of 36,000x corresponding to a physical pixel size of 1.15 Å/pixel. A total of 1,895 movies (68 frames/movie) of cross-linked MCU_{NC} and 2,444 movies (64 frames/movie) of native MCU_{NC} were collected by navigating to the center of four holes and image shifting ~2 μm to each exposure target. Movies were collected using a 17 second exposure (cross-linked MCU_{NC}) or 16 second exposure (native MCU_{NC}) with an exposure rate of ~5.2 e^-/pixel/s, resulting in a total exposure of ~64-66 e^-/Å^2 and a nominal defocus range from -1 μm to -2 μm. The MotionCor2 frame alignment program (*40*) was used to perform motion correction and dose-weighting as part of the Appion pre-processing workflow. Frame alignment was performed on 5 x 5 tiled frames with a B-factor of 100 applied. Unweighted summed images were used for CTF determination using CTFFIND4 (*36*).

Cross-linked MCU_{NC} in nanodiscs

Difference of Gaussians (DoG) picker (*37*) was used to automatically pick particles from the dose-weighted micrographs yielding a stack of 537,583 particles that were binned 4 × 4 (4.6 Å/pixel, 64 pixel box size) and subjected to reference-free 2D classification using RELION 2.1 (*41*). A total of 230,776 particles corresponding to the 2D classes that displayed the strongest secondary-structural elements were input to *ab-initio* refinement in cryoSPARC (*42*) to generate an initial model. The best 7 classes were then used for template-based automated particle picking against the whole dataset using RELION. A total of 1,895,054 particles were extracted from these micrographs and binned 4 x 4 (4.6 Å/pixel, 64-pixel box size). Reference-free 2D classification in RELION was then used to sort out non-particles and poor-quality picks in the data. A total of 555,365 particles corresponding to the best 2D class averages were input to 3D auto-refinement in RELION without symmetry imposed. The previously generated *ab-initio* volume was low-pass filtered to 30 Å and used as an initial model. The refined volume (~9.2 Å) was subjected to 3D classification (k=6, tau_fudge=12) with a soft mask (5-pixel extension, 5-pixel soft cosine edge) to further sort out non-particles or poor-quality picks. A total of 365,294 particles contributing to the best-resolved 3D classes were re-extracted binned 2 x 2 (2.3 Å/pixel, 128-pixel box size) and 3D auto-refined with a soft mask to ~5.3 Å resolution. These particles were then subjected to an additional round of 3D classification, unbinned auto-refinement, and 3D classification without angular or translational searches to obtain a final ~3.7 Å reconstruction (45,636 particles, C2 symmetry) as determined by gold-standard 0.143 Fourier shell correlation (FSC) (*43*).

Native MCU_{NC} in amphipol

Similar automated particle picking, 2D classification, 3D classification and auto-refinement strategies as those described above were applied to the data collected of native MCU_{NC} using RELION. The cross-linked MCU_{NC} reconstruction was low-pass filtered to 30 Å and used

as an initial model for 3D refinement. Asymmetric refinement of three states from MCU_{NC} prepared at low calcium yielded ~7.5 Å (28,148 particles), ~7.4 Å (29,540 particles), and ~5.1 Å (27,884 particles) reconstructions. A single state, exhibiting C2 symmetry, from MCU_{NC} prepared at high calcium was refined to ~4.7 Å (45,188 particles). The resolutions of all reconstructions were calculated using gold-standard 0.143 FSC.

Since the native and cross-linked MCU_{NC} reconstructions were structurally similar, both datasets were combined in an effort to obtain an improved map. Briefly, 2D classification and one round of 3D classification was performed separately for the native and cross-linked data (see above) to remove poor-quality particles prior to combining the data. A total of 580,600 particles (215,306 particles of native MCU_{NC} and 365,294 particles of cross-linked MCU_{NC}) were 3D auto-refined binned 2 x 2 (2.3 Å/pixel, 128-pixel box size) without symmetry imposed to yield a ~4.6 Å reconstruction. 3D classification (k=8, tau_fudge=12) without angular or translation searches was performed using a soft mask generated from the entire volume that excluded the density around the transmembrane region. One class was re-centered, re-extracted without binning (1.15 Å/pixel, 256-pixel box size) with duplicate particles removed, and subsequently auto-refined to ~3.8 Å with C2 symmetry imposed. A final round of 3D classification (k=2, tau_fudge=25) without angular or translational searches was performed to obtain a single class consisting of 36,537 particles. Approximately 80% of the particles in this final stack came from the cross-linked MCU_{NC} data. 3D auto-refinement of these particles with C2 symmetry imposed yielded a ~3.7 Å reconstruction as determined by gold-standard 0.143 FSC. The quality of the combined map showed improvements in several regions of the density, particularly in the transmembrane region, compared to the cross-linked reconstruction alone and therefore was used for model-building. The fact that only 6% of the particles resulting from 2D and 3D classification were included in the final reconstruction suggests that the MCU channel has a complex conformational landscape that does not strictly adhere to the imposed C2 symmetry. Through classification we have likely selected the subset of particles that are the most C2-symmetric in conformation, but the moderate resolution of our final reconstruction also indicates that even these particles are conformationally labile. Advances in data processing algorithms and data collection strategies will eventually enable us to fully integrate all the structural information contained within our images to more completely describe the conformational landscapes of these macromolecules.

Model building and refinement

The MCU_{NC} model was built *de novo* into the electron density map in Coot (*44*). Ideal secondary structures were placed and rigid body fitted into the density. Bulky side chains were assigned to guide the correct helical register. Additional side chains were built into the density in optimal rotamer conformations. Loops connecting secondary structures were subsequently built as much as possible. To facilitate model building of the N-terminal domain (NTD), the crystal structure of the NTD from human MCU (PDB ID: 4XTB) was docked to the cryo-EM density map. During the initial manual model building, ideal geometric restraints in the backbone and rotamer conformations were imposed as much as possible in Coot. One Ca^{2+} ion was placed into the electron density along the ion conduction pore at Site 2. The Ca^{2+} coordination restraints were generated by eLBOW (*45*). After manual model building, the structural model was subjected to real-space refinement via the graphical interface in PHENIX against the cryo-EM map (*46*). Rigid-body and global-minimization refinement was used along with secondary-structure and ion-coordination restraints. The real-space refined structure was analyzed using the Molprobity server (http://molprobity.biochem.duke.edu/) (*47*) and problematic regions were manually fixed in Coot.

FSCs of the half maps against the refined model agree with each other, suggesting that the model is not over-refined (fig. S3). The model contained amino acids 107-441 with several loops missing (127-151, 180-185, 195-248, 381-394), covering about 53% of the construct.

Cell culture and transfections

Human MCU (hMCU) knock-out (KO) cell line was generated by CRISPR/Cas9 (*48*) (Functional Genomics Shared Resource, Duke university) and confirmed by western blot with anti-hMCU antibody (Sigma-Aldrich). Both hMCU-KO cell line and wildtype (WT) HEK293T cells (ATCC) were grown in DMEM supplemented with 10% FBS (Gibco), 1% penicillin/streptomycin (Gibco) and were maintained in 5% CO_2 at 37°C. Cells were grown in 10-cm dishes and were transiently transfected at 90-95% confluency. 8 μg pEG BacMam plasmid encoding human MCU (hMCU) wildtype or mutants were transfected into hMCU-KO cell line with Lipofectamine 2000 following manufacturer's instructions (Invitrogen). 24 h post-transfection, cells were harvested for calcium uptake assay and western blot. Site-directed mutagenesis of hMCU was performed using the QuikChange mutagenesis kit (Agilent).

Mitochondrial calcium uptake assay

Calcium uptake assay was performed as described previously (*11*). Transfected cells (see above) were harvested by centrifugation at 1710 rpm for 5 min and re-suspended in wash buffer (25 mM HEPES, 120 mM KCl, 2 mM KH_2PO_4, 1 mM $MgCl_2$, 50 mM, EGTA, pH 7.2-KOH). The cells were pelleted again and re-suspended in recording buffer (25 mM HEPES, 120 mM KCl, 2 mM KH_2PO_4, 1 mM $MgCl_2$, 5 mM succinate, pH 7.2-KOH). Cell suspension was loaded to a cuvette containing a stir bar. To monitor the Ca^{2+} uptake by cells, reagents were added to the stirred cuvette in the following order: 0.5 μM Calcium green-5N (Invitrogen), 30 μM digitonin (Sigma-Aldrich), 10 μM $CaCl_2$. To inhibit the Ca^{2+} uptake, 2 μM Ru360 (Calbiochem) was added prior to 10 μM $CaCl_2$. The fluorescence was recorded using a Cary Eclipse Fluorescence spectrophotometer (Agilent Technologies) with ex: 506 nm, ex-slit: 5 nm, em: 529 nm, em-slit: 5 nm every 30 s at 37°C followed by data analysis.

Western blot

Transfected cells (see above) were lysed with RIPA buffer (Sigma-Aldrich) and were spun down at 12000 rpm at 4°C for 30 min. The supernatant was collected and loaded to 4-15 % SDS-PAGE (Bio-Rad) and transferred onto PVDF membrane (Bio-Rad). The membrane was washed 3 times with PBS buffer supplemented with 5% Tween 20 (PBST), blocked with 5% skim milk (Bio-Rad) at 4°C for 16 h. After washing 3 times with PBST, the membrane was incubated with the primary anti-FLAG antibody (1:1000 dilution in PBST, Sigma-Aldrich) or anti-β-actin antibody (1:1000 dilution in PBST, Cell Signaling Technology) for 1 h at room temperature. After washing 3 times with PBST, membrane was incubated with the secondary antibody IRDye-800CW (1:10000 dilution in PBST, Li-Cor Biosciences) followed by washing 2 times with PBST and washing once with PBS. The membrane was imaged by Odyssey® CLx Imaging System (Li-Cor Biosciences).

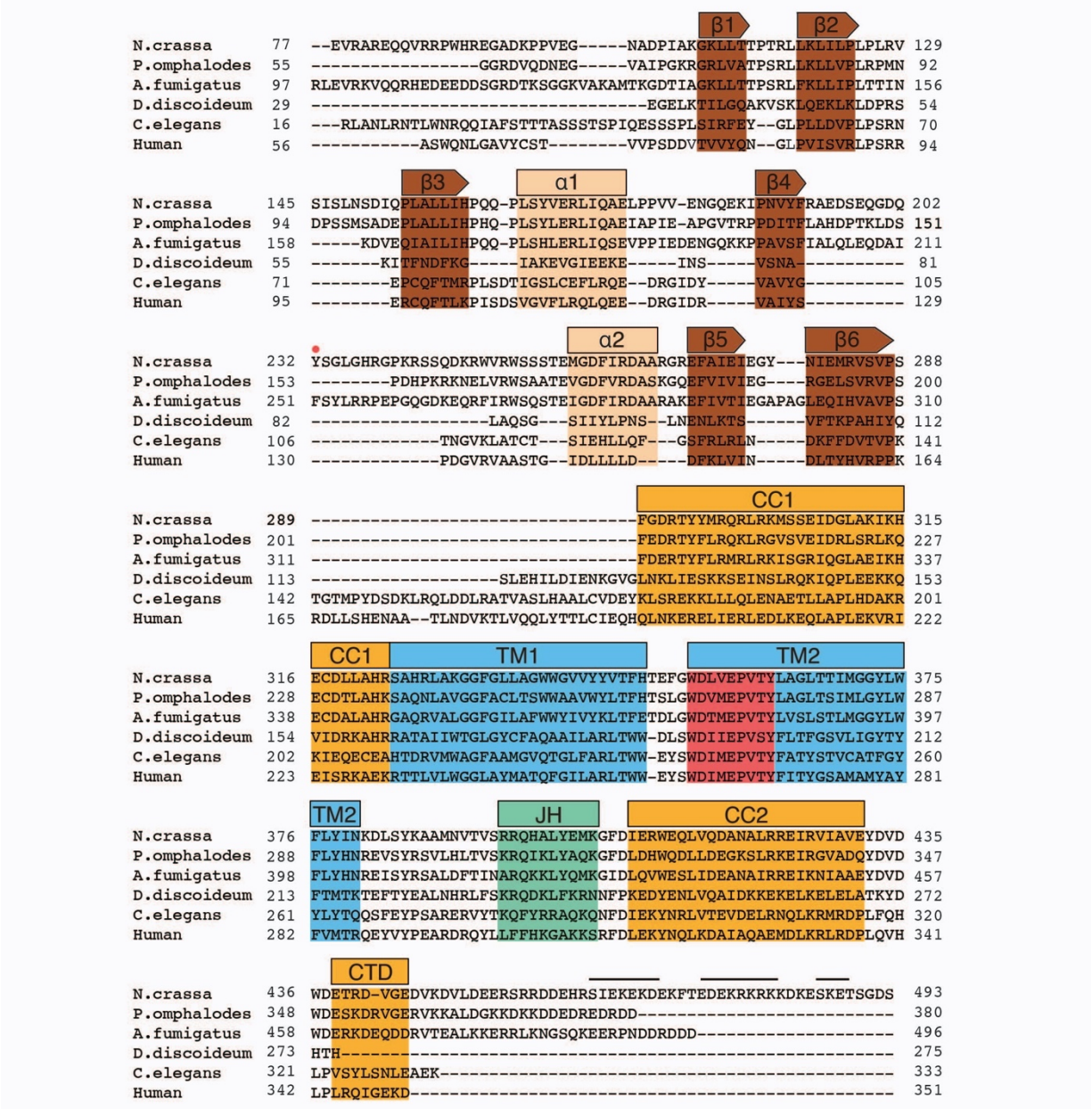

Fig. S1. Structure-based sequence alignment of MCU orthologues. Secondary structures in MCU_{NC} structure are indicated by rectangles (helices) and arrows (β-strands) and colored as in Figure 1. The conserved "WDΦΦEPVTY" motif is highlighted in red. *N. crassa* MCU shares high sequence homology with the two fungal orthologues, *P. omphalodes* and *A. fumigatus* MCU, which have been functionally characterized (*17, 18*). The Y232A point mutation which prevents proteolysis is denoted by a red dot. The three putative helices absent in human MCU are indicated by lines for MCU_{NC} based on secondary structure prediction.

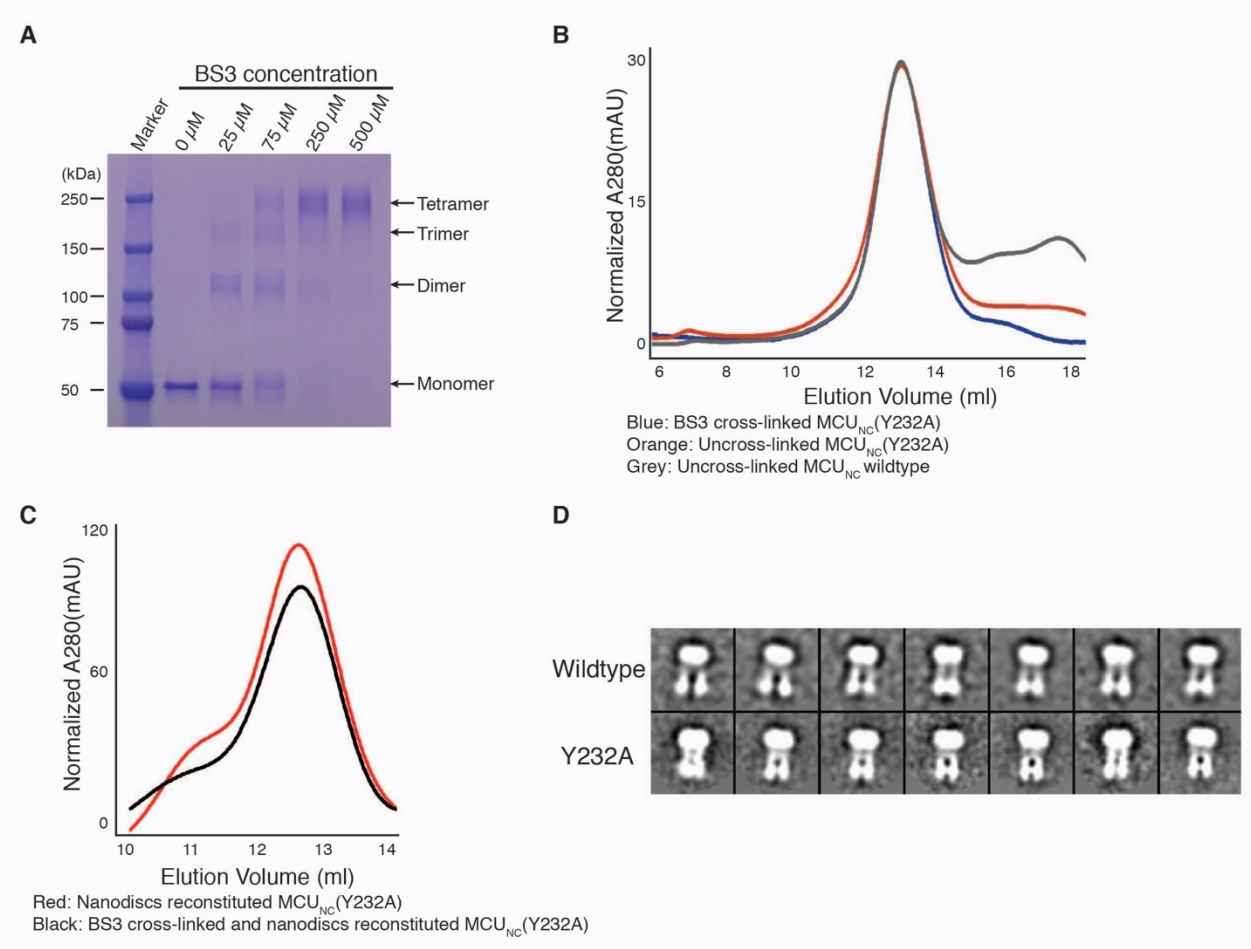

Fig. S2. Biochemical analysis of the oligomeric state of MCU_{NC}. (**A**) Chemical cross-linking of MCU_{NC} by BS3. 0.25 mg ml^{-1} protein purified in DDM was mixed with BS3 at a working concentration of 0, 25, 75, 250, 500 μM respectively in a reaction volume of 20 μl and incubated at room temperature for 30 min. The reactions were quenched with 50 mM Tris-HCl pH 8.0 and 5 μl from each reaction was analyzed on 4-15% SDS-PAGE. Increase in BS3 results in a single oligomeric state of MCU_{NC} that is most compatible with the tetramer. (**B**) Purification of MCU_{NC} (Y232A) in 1mM DDM without (orange) and with (blue) cross-linking by 250 μM BS3, and of uncross-linked MCU_{NC} wildtype (grey) in 1mM DDM by size-exclusion chromatography. The identical elution volumes suggest that neither mutation nor cross-linking affects the oligomeric state of MCU_{NC} (A). Absorbance at 280nm was normalized against BS3 cross-linked MCU_{NC} (Y232A) (blue). (**C**) Purification of MCU_{NC} (Y232A) reconstituted in nanodiscs without (red) and with (black) cross-linking by 250 μM BS3. Absorbance at 280nm was normalized against nanodiscs reconstituted MCU_{NC} (Y232A) (red). (**D**) Negative stain 2D classes of wild-type MCU_{NC} (top) and Y232A MCU_{NC} (bottom).

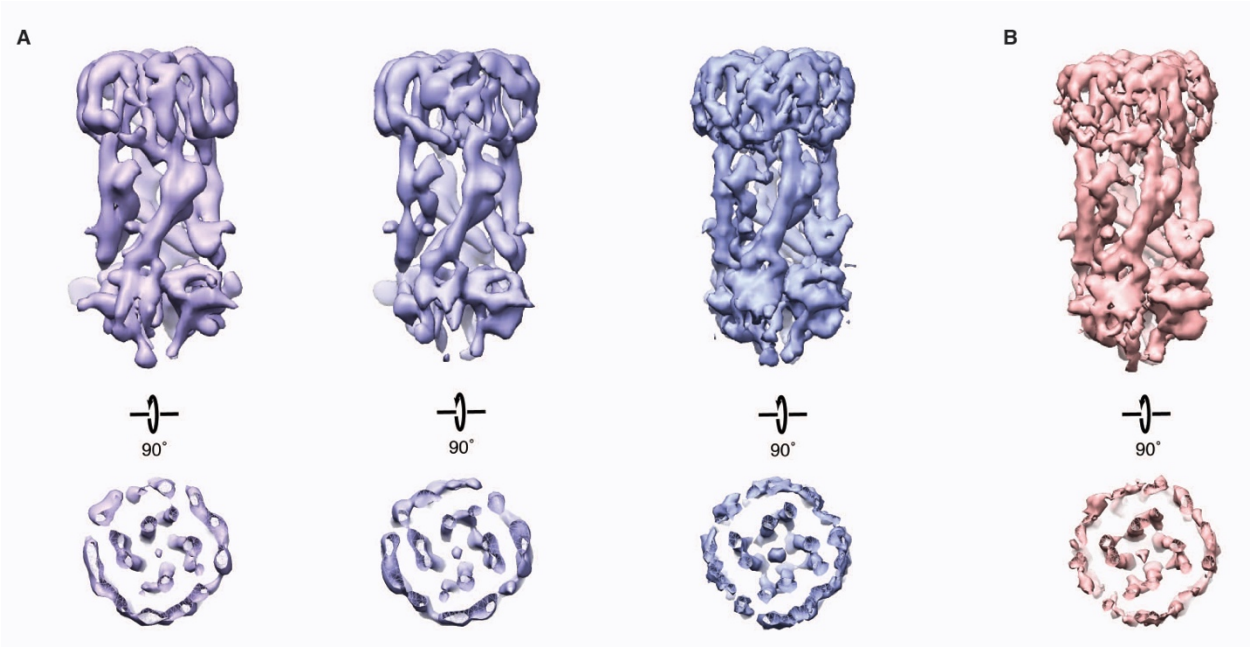

Fig. S3. Cryo-EM reconstruction of MCU_{NC} in amphipol at low and high concentrations of Ca^{2+}. Orthogonal views of asymmetric reconstructions of MCU_{NC} purified at **(A)** low Ca^{2+} and **(B)** high Ca^{2+} displaying the tetrameric arrangement of the channel (see Methods).

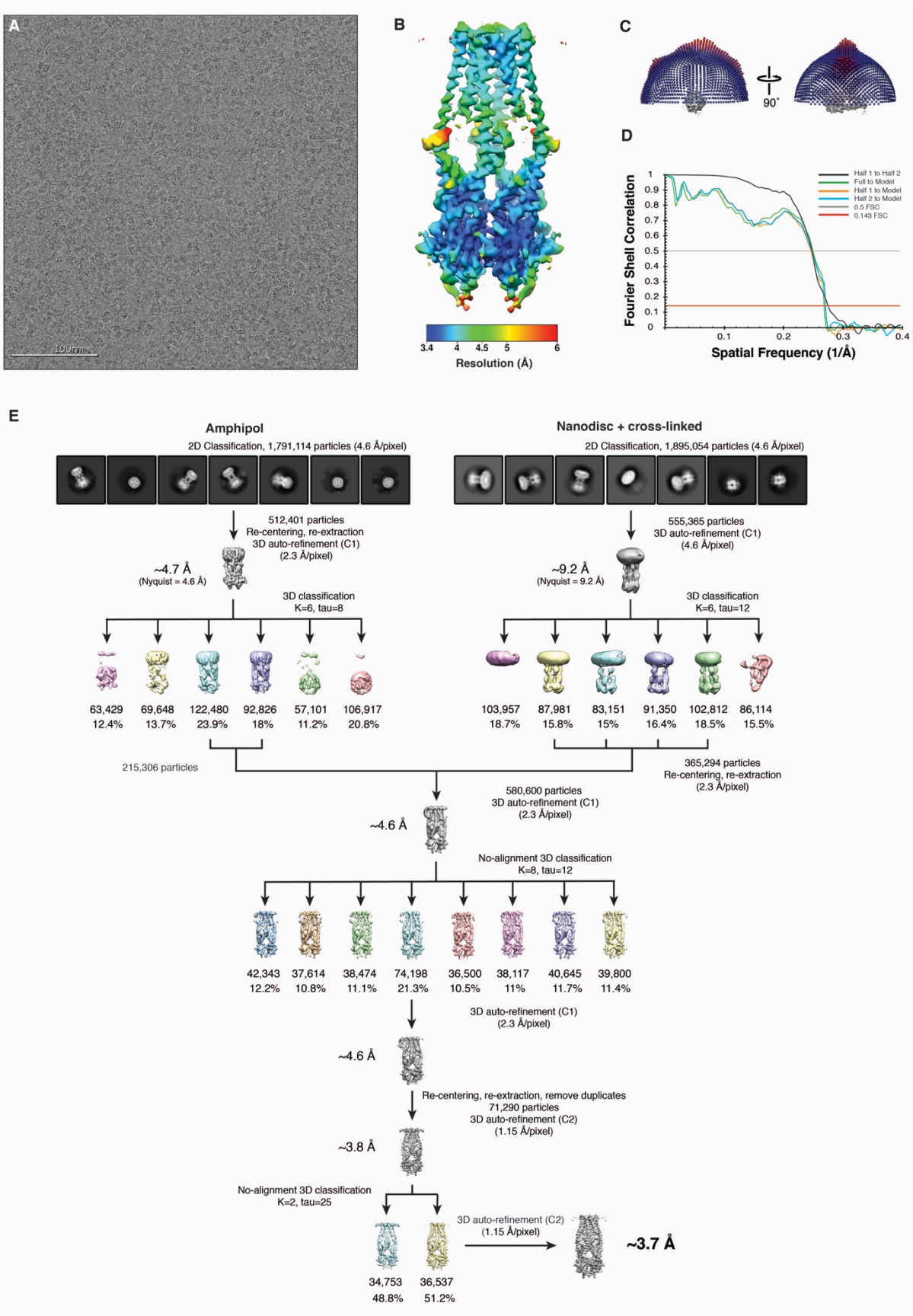
A
100nm
B
3.4
4
4.5
5
6
Resolution (Å)
C
90°
D
Fourier Shell Correlation
Spatial Frequency (1/Å)
Half 1 to Half 2
Full to Model
Half 1 to Model
Half 2 to Model
0.5 FSC
0.143 FSC
E
Amphipol
2D Classification, 1,791,114 particles (4.6 Å/pixel)
512,401 particles
Re-centering, re-extraction
3D auto-refinement (C1)
(2.3 Å/pixel)
~4.7 Å
(Nyquist = 4.6 Å)
3D classification
K=6, tau=8
63,429
12.4%
69,648
13.7%
122,480
23.9%
92,826
18%
57,101
11.2%
106,917
20.8%
215,306 particles
Nanodisc + cross-linked
2D Classification, 1,895,054 particles (4.6 Å/pixel)
555,365 particles
3D auto-refinement (C1)
(4.6 Å/pixel)
~9.2 Å
(Nyquist = 9.2 Å)
3D classification
K=6, tau=12
103,957
18.7%
87,981
15.8%
83,151
15%
91,350
16.4%
102,812
18.5%
86,114
15.5%
365,294 particles
Re-centering, re-extraction
(2.3 Å/pixel)
580,600 particles
3D auto-refinement (C1)
(2.3 Å/pixel)
~4.6 Å
No-alignment 3D classification
K=8, tau=12
42,343
12.2%
37,614
10.8%
38,474
11.1%
74,198
21.3%
36,500
10.5%
38,117
11%
40,645
11.7%
39,800
11.4%
3D auto-refinement (C1)
(2.3 Å/pixel)
~4.6 Å
Re-centering, re-extraction, remove duplicates
71,290 particles
3D auto-refinement (C2)
(1.15 Å/pixel)
~3.8 Å
No-alignment 3D classification
K=2, tau=25
34,753
48.8%
36,537
51.2%
3D auto-refinement (C2)
(1.15 Å/pixel)
~3.7 Å

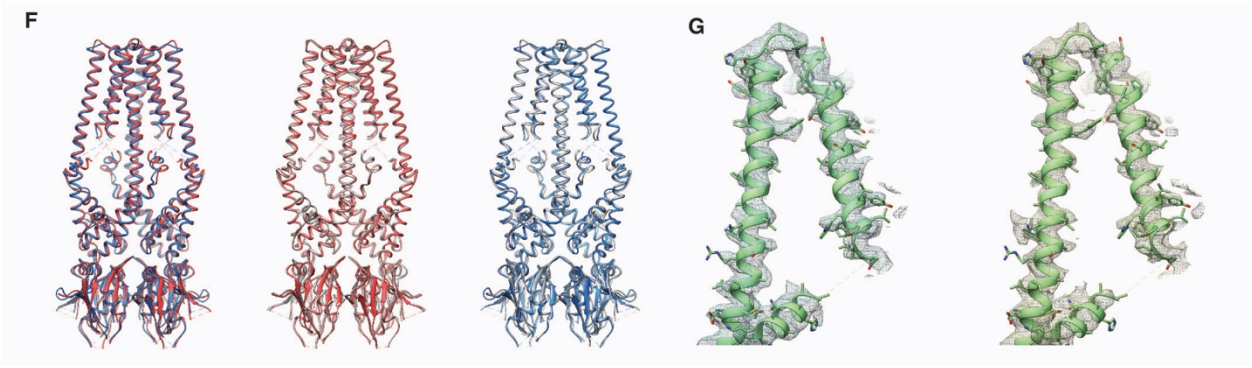

Fig. S4. Cryo-EM structure determination. (A) Representative micrograph of cross-linked MCU_{NC} in lipid nanodiscs embedded in vitreous ice. **(B)** Local resolution estimates of the final reconstructions calculated using BSOFT (*49*). **(C)** Euler distribution plot for the final reconstruction. **(D)** FSC curves calculated between the half maps (black line), atomic model and the final map (green line), and between the model and each half-map (orange and blue lines). **(E)** Particles were extracted from aligned micrographs of native MCU_{NC} in amphipol and cross-linked MCU_{NC} in nanodiscs, Fourier binned 2 x 2 and 4 x 4, respectively, and subjected to reference-free 2D classification using RELION. Representative 2D class averages are shown. Particles comprising the "best" class averages were 3D auto-refined without symmetry and subjected to 3D classification. For each class, the number of contributing particles and percentage relative to total particles input to classification are listed below, respectively. A total of 580,600 particles corresponding to the best-resolved classes from both datasets were combined and 3D auto-refined together to yield a ~4.6 Å resolution reconstruction. Particles were subjected to two rounds of no-alignment classification to obtain a final subset of 36,537 particles, which was auto-refined with C2 symmetry enforced to yield a final reconstruction at ~3.7 Å resolution. **(F)** Overlay of models (shown in ribbon representation) built from the following cryo-EM reconstructions: native MCU_{NC} with cross-linked MCU_{NC} (left), native MCU_{NC} with final combined MCU_{NC} (center), cross-linked MCU_{NC} with final combined MCU_{NC} (right) showing the significantly structural similarities between the reconstructions. Models of native, cross-linked, and combined MCU_{NC} are colored red, blue, and grey, respectively. **(G)** Comparison of the density quality of the transmembrane domain (shown as ribbon) between the final combined (left) and cross-linked (right) MCU_{NC} reconstructions (see Methods).

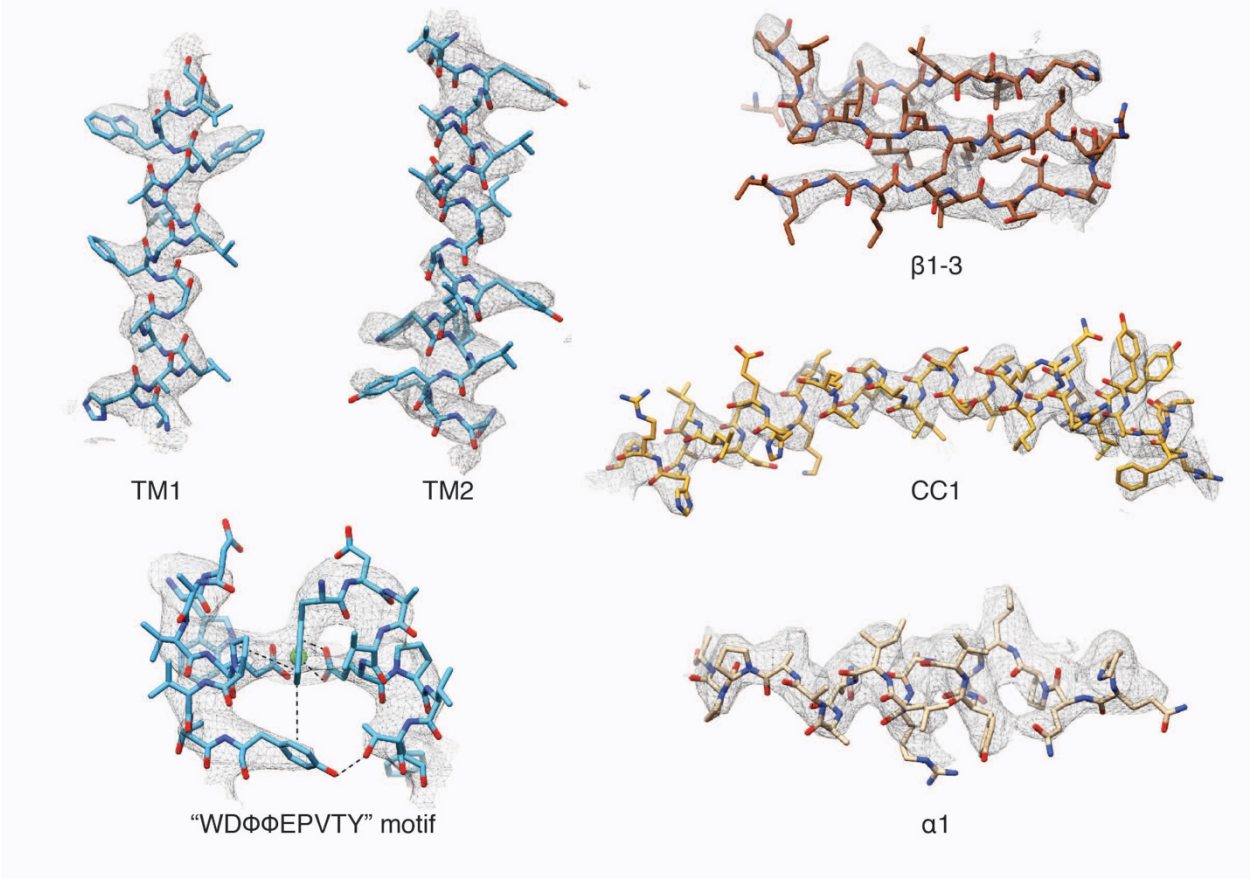

Fig. S5. Quality of electron density of key elements in the structure of MCU_{NC}. The structural elements are labeled and colored according to Fig. 1, and shown as sticks. The electron density is shown as a gray mesh, zoned ~2 Å around atoms.

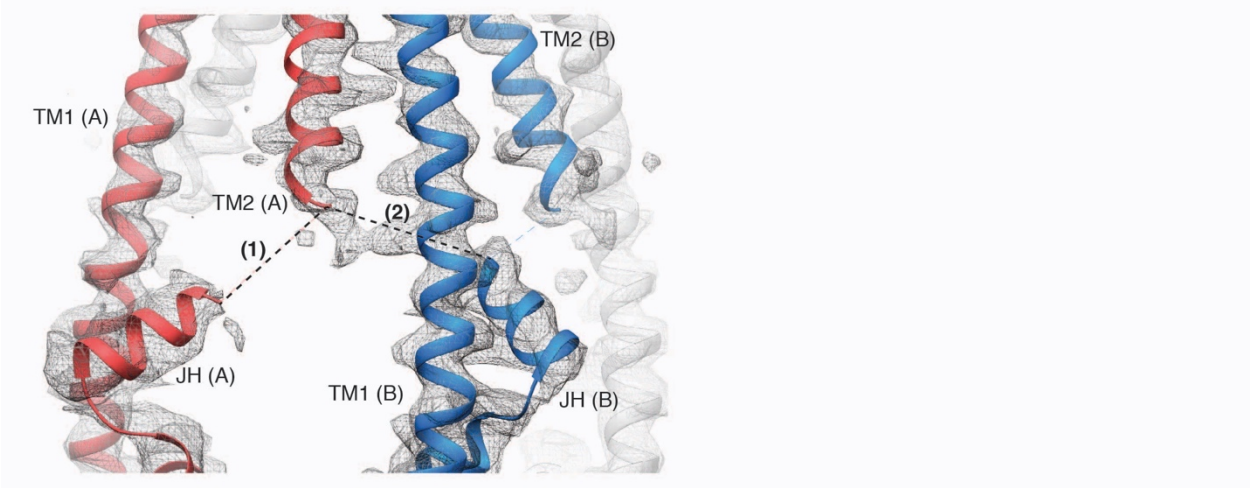

Fig. S6. Uncertainty in the connection between TMD and CCD. Cryo-EM density of the MCU_{NC} structure (gray mesh) viewed from the side shows ambiguous connecting density between TM2 and JH of protomer A (red ribbon) and JH of protomer B (blue ribbon), indicated by dashed lines (1) and (2), suggesting a possible "domain-swapped" configuration within the TMD.

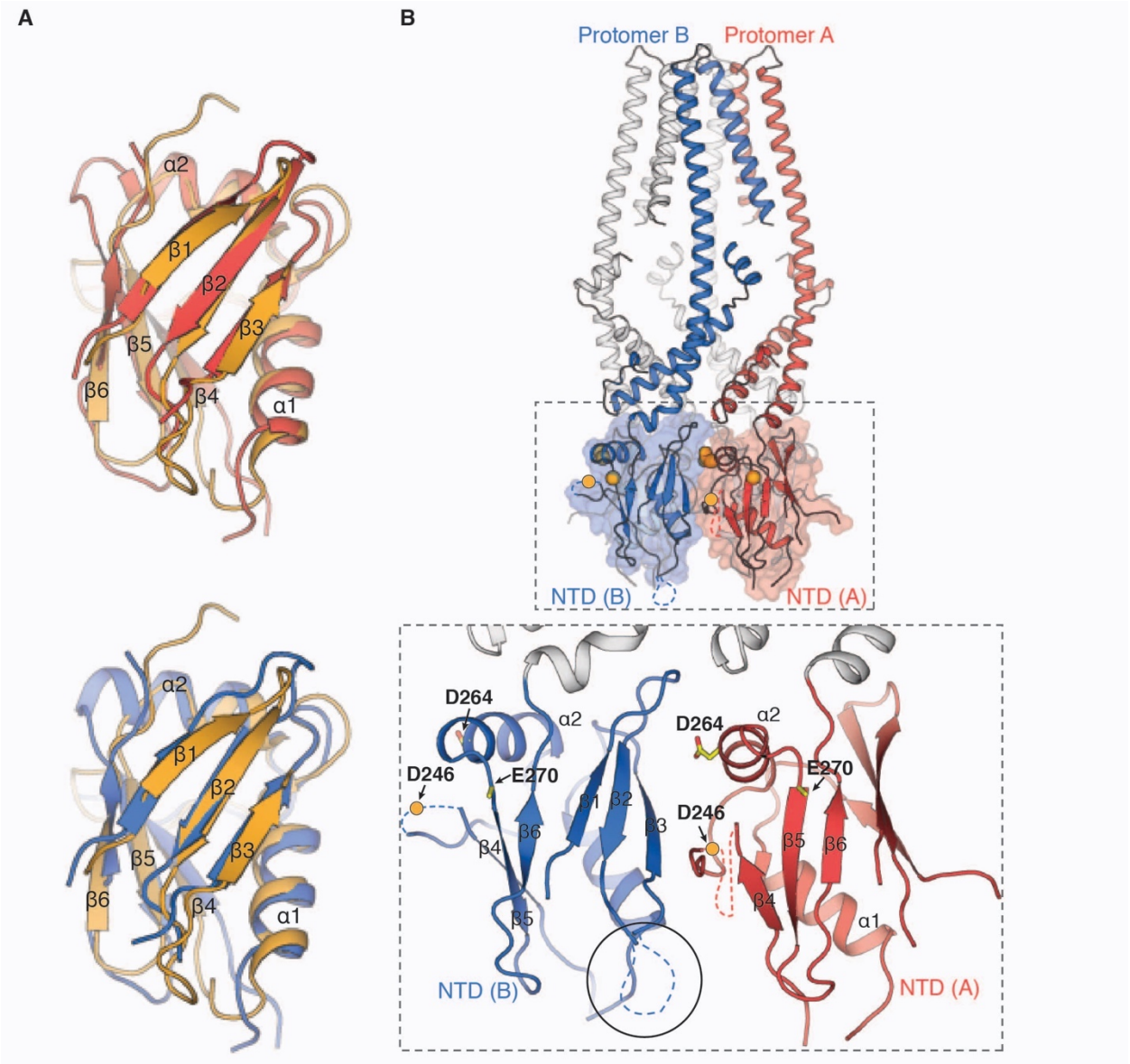

Fig. S7. Structural comparison of NTD from MCU_{NC} and human MCU. (**A**) The NTD from protomer A (red) and from protomer B (blue) of MCU_{NC} superimposes well on the crystal structure of the NTD from human MCU (orange, PDB ID: 5KUJ). (**B**) The putative divalent cation binding pocket and phosphorylation site at the NTD of MCU_{NC}. Asp^{246}, Asp^{264}, and Glu^{270} form an acidic patch for the potential binding of divalent cations. Side chains are shown as yellow sticks, while Asp^{246} not modeled in the structure is denoted as an orange sphere. The putative phosphorylation site is located on the loop (dashed line) connecting β2 and β3.

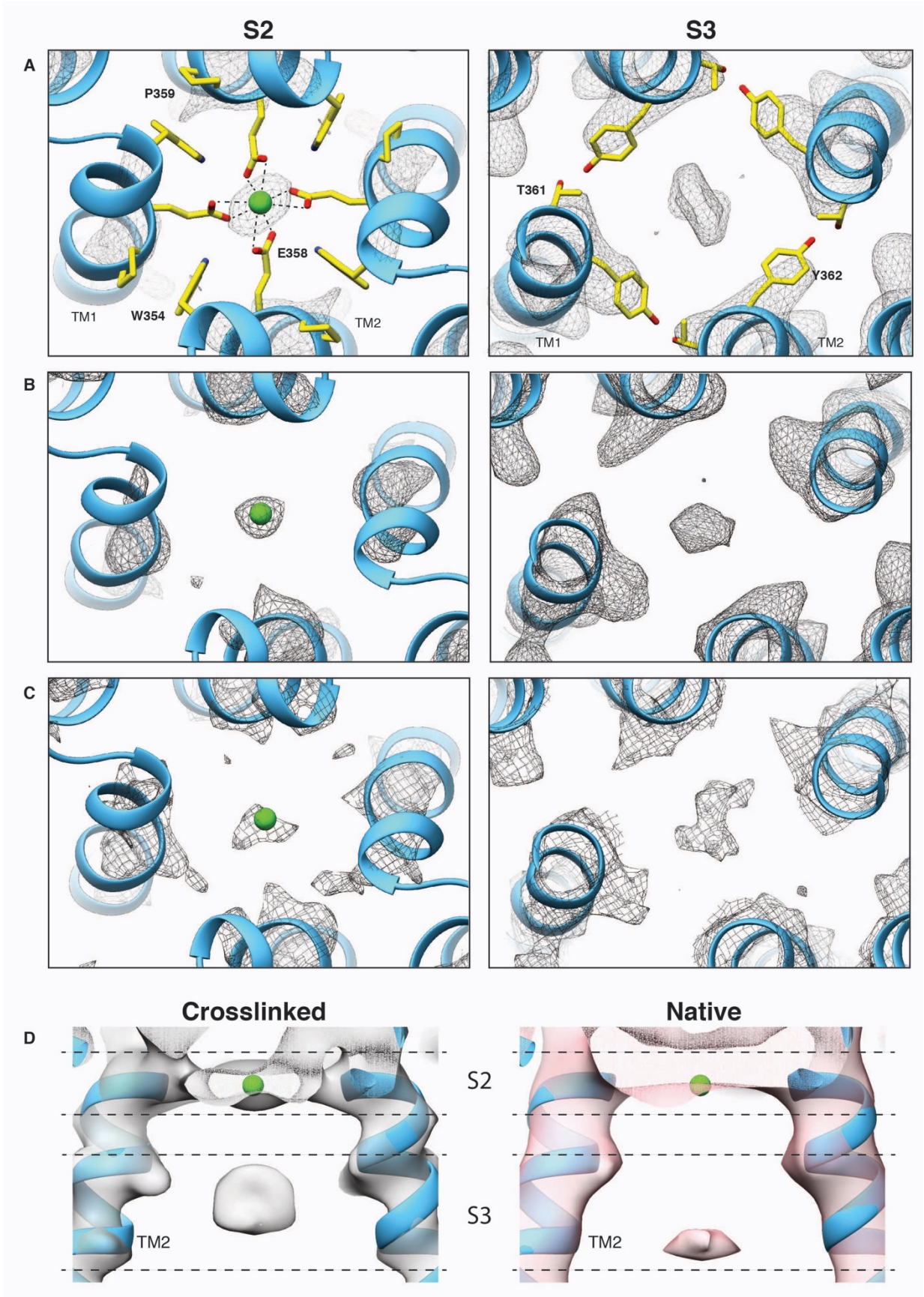
S2
S3
A
P359
E358
TM1
W354
TM2
T361
Y362
TM1
TM2
B
C
Crosslinked
Native
D
S2
S3
TM2
TM2

Fig. S8. Putative Ca^{2+} and unassigned EM density peaks at the selectivity filter. Cryo-EM density at the putative Ca^{2+} coordination site S2 (left, grey mesh; sigma=17.3) and "S3" (right, grey mesh; sigma=9.4) is present in **(A)** the final reconstruction of MCU_{NC}, **(B)** the asymmetric reconstruction, and **(C)** both half maps (only half map 1 shown here, sigma=12.2 and 7.4 at S2 and "S3", respectively). Views and residues involved in Ca^{2+} coordination at S2 and polar residues putatively involved at "S3" are represented and colored according to Fig. 4C. **(D)** Densities at S2 and "S3" are present in both cross-linked (left, sigma=9.4) and native (right, sigma=9.7) MCU_{NC} reconstructions. The position of the unknown density at "S3" differs between the cross-linked and native structures.

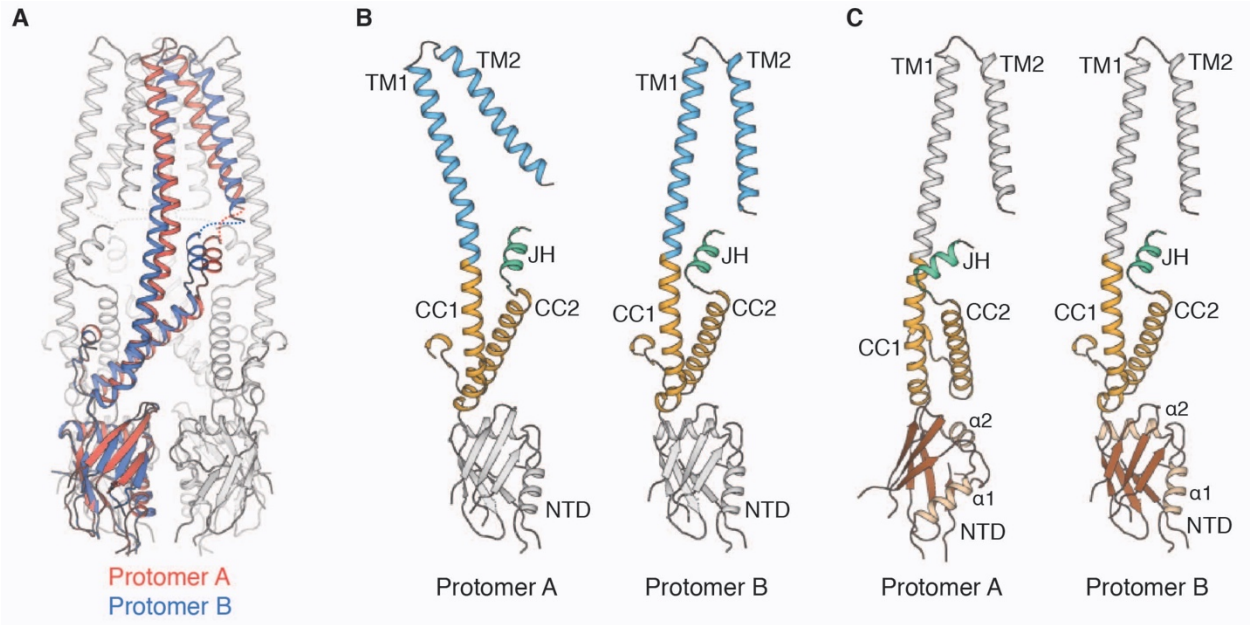

Fig. S9. Structural comparison of protomer A and protomer B in MCU_{NC}. (**A**) Superimposition of protomer B (blue) over protomer A (red) in the context of the tetrameric MCU_{NC} structure. (**B and C**) Side-by-side comparison of protomer A (red) and protomer B (blue) at NTD (**B**) and at TMD (**C**), showing the rigid body rotations of TMD and NTD around the hinge point at JH.

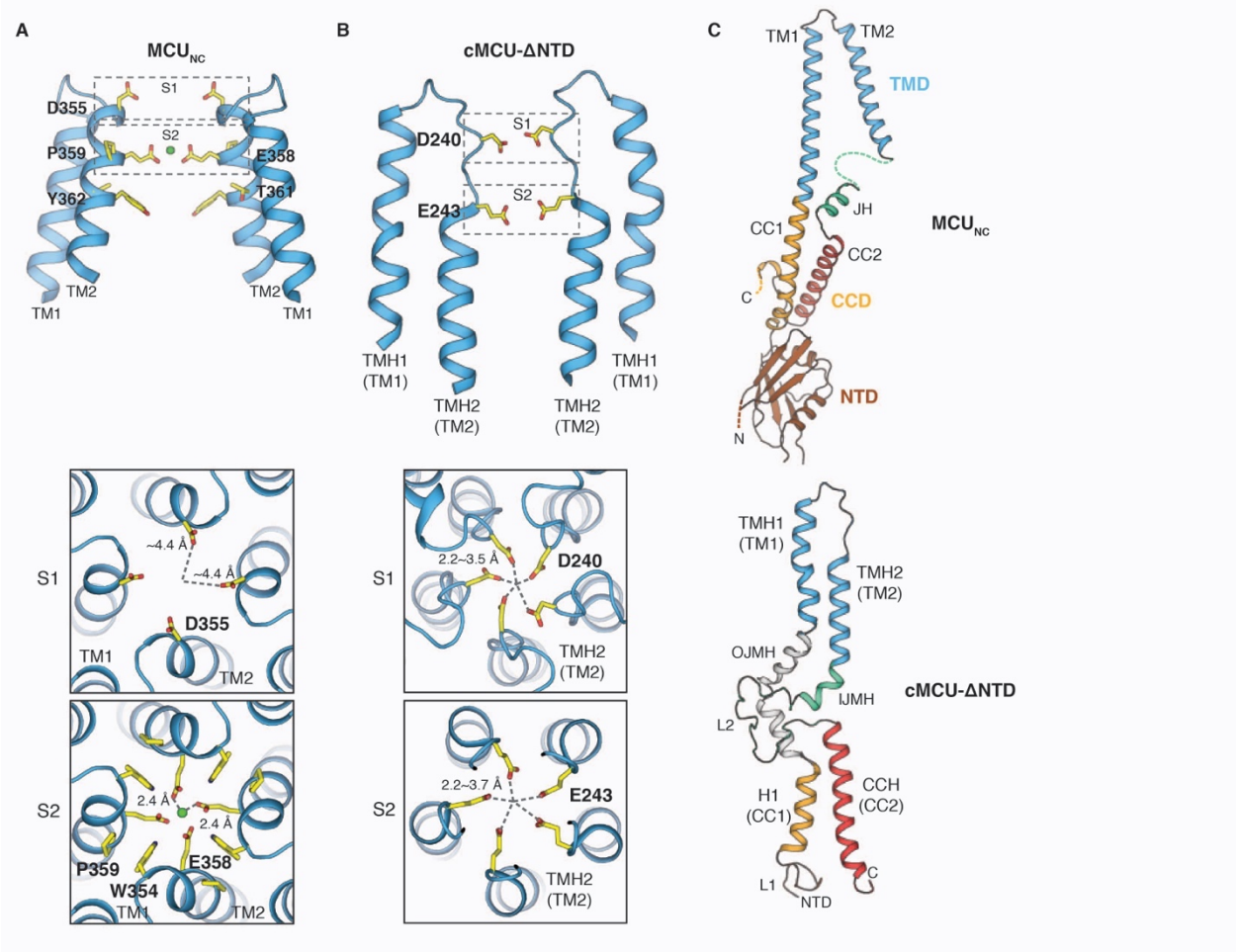

Fig. S10. Comparison of the ion conduction pore between MCU$_{NC}$ and cMCU-ΔNTD structures. (**A and B**) Comparison of the calcium coordination sites in MCU$_{NC}$ and cMCU-ΔNTD (PDB ID: 5ID3) and the corresponding close-up views from the intermembrane space. The approximate radii at S1 and S2 in MCU$_{NC}$ and cMCU-ΔNTD are indicated. (**C**) Comparison of the protomer structure between MCU$_{NC}$ and cMCU-ΔNTD.

	Amphipol	Cross-linked Nanodiscs
Data collection		
Microscope	Talos Arctica	Talos Arctica
Voltage (keV)	200	200
Nominal magnification*	36,000x	36,000x
Electron dose (e^{-} Å^{-2})	64	66
Exposure rate (e^{-}/pixel/sec)	5.2	5.2
Detector	K2 Summit	K2 Summit
Pixel size (Å)*	1.15	1.15
Defocus range (μm)	-1.2 to -2.0	-1.0 to -2.0
Total extracted particles (no.)	1,791,114	1,895,054
Refined particles (no.)	512,401	555,365
Combined particles (no.)	215,306	365,294
Reconstruction		
Final particles (no.)	36,537	
Symmetry imposed	C2	
Resolution (global)	3.68	
FSC 0.5 (unmasked/masked)	6.93/4.03	
FSC 0.143 (unmasked/masked)	4.53/3.68	
Applied B-factor (Å^{2})	-110	
Refinement		
Protein residues	944	
Ligand/ ion	1	
Map Correlation Coefficient	0.78	
R.m.s. deviations		
Bond lengths (Å)	0.00	
Bond angles (°)	0.71	
Ramachandran		
Outliers	0.00 %	
Allowed	3.10 %	
Favored	96.90 %	
Poor rotamers (%)	0	
MolProbity score	1.11	
Clashscore (all atoms)	1.74	

*Calibrated pixel size at the detector

Table S1. Data collection, reconstruction, and model refinement statistics of MCU_{NC}.

1. C. Mammucari, G. Gherardi, R. Rizzuto, Structure, Activity Regulation, and Role of the Mitochondrial Calcium Uniporter in Health and Disease. *Front Oncol* **7**, 139 (2017).
2. K. J. Kamer, V. K. Mootha, The molecular era of the mitochondrial calcium uniporter. *Nat Rev Mol Cell Biol* **16**, 545-553 (2015).
3. T. E. Gunter, D. R. Pfeiffer, Mechanisms by which mitochondria transport calcium. *Am J Physiol* **258**, C755-786 (1990).
4. Y. Kirichok, G. Krapivinsky, D. E. Clapham, The mitochondrial calcium uniporter is a highly selective ion channel. *Nature* **427**, 360-364 (2004).
5. J. M. Baughman *et al.*, Integrative genomics identifies MCU as an essential component of the mitochondrial calcium uniporter. *Nature* **476**, 341-345 (2011).
6. F. Perocchi *et al.*, MICU1 encodes a mitochondrial EF hand protein required for Ca(2+) uptake. *Nature* **467**, 291-296 (2010).
7. D. De Stefani, A. Raffaello, E. Teardo, I. Szabo, R. Rizzuto, A forty-kilodalton protein of the inner membrane is the mitochondrial calcium uniporter. *Nature* **476**, 336-340 (2011).
8. Y. Sancak *et al.*, EMRE is an essential component of the mitochondrial calcium uniporter complex. *Science* **342**, 1379-1382 (2013).
9. A. Raffaello *et al.*, The mitochondrial calcium uniporter is a multimer that can include a dominant-negative pore-forming subunit. *EMBO J* **32**, 2362-2376 (2013).
10. K. J. Kamer, V. K. Mootha, MICU1 and MICU2 play nonredundant roles in the regulation of the mitochondrial calcium uniporter. *EMBO Rep* **15**, 299-307 (2014).
11. M. F. Tsai *et al.*, Dual functions of a small regulatory subunit in the mitochondrial calcium uniporter complex. *Elife* **5**, (2016).
12. N. E. Hoffman *et al.*, MICU1 motifs define mitochondrial calcium uniporter binding and activity. *Cell Rep* **5**, 1576-1588 (2013).
13. K. J. Kamer, Z. Grabarek, V. K. Mootha, High-affinity cooperative Ca(2+) binding by MICU1-MICU2 serves as an on-off switch for the uniporter. *EMBO Rep* **18**, 1397-1411 (2017).
14. G. Csordas *et al.*, MICU1 controls both the threshold and cooperative activation of the mitochondrial Ca(2)(+) uniporter. *Cell Metab* **17**, 976-987 (2013).
15. K. Mallilankaraman *et al.*, MICU1 is an essential gatekeeper for MCU-mediated mitochondrial Ca(2+) uptake that regulates cell survival. *Cell* **151**, 630-644 (2012).
16. A. G. Bick, S. E. Calvo, V. K. Mootha, Evolutionary diversity of the mitochondrial calcium uniporter. *Science* **336**, 886 (2012).
17. E. Kovacs-Bogdan *et al.*, Reconstitution of the mitochondrial calcium uniporter in yeast. *Proc Natl Acad Sci U S A* **111**, 8985-8990 (2014).
18. J. Song, X. Liu, P. Zhai, J. Huang, L. Lu, A putative mitochondrial calcium uniporter in A. fumigatus contributes to mitochondrial Ca(2+) homeostasis and stress responses. *Fungal Genet Biol* **94**, 15-22 (2016).
19. G. Wu *et al.*, Single channel recording of a mitochondrial calcium uniporter. *Biochem Biophys Res Commun* **496**, 127-132 (2018).
20. Y. Lee *et al.*, Structure and function of the N-terminal domain of the human mitochondrial calcium uniporter. *EMBO Rep* **16**, 1318-1333 (2015).
21. S. K. Lee *et al.*, Structural Insights into Mitochondrial Calcium Uniporter Regulation by Divalent Cations. *Cell Chem Biol* **23**, 1157-1169 (2016).
22. K. Oxenoid *et al.*, Architecture of the mitochondrial calcium uniporter. *Nature* **533**, 269-273 (2016).
23. X. Hou, L. Pedi, M. M. Diver, S. B. Long, Crystal structure of the calcium release-activated calcium channel Orai. *Science* **338**, 1308-1313 (2012).
24. K. Saotome, A. K. Singh, M. V. Yelshanskaya, A. I. Sobolevsky, Crystal structure of the epithelial calcium channel TRPV6. *Nature* **534**, 506-511 (2016).
25. D. A. Doyle *et al.*, The structure of the potassium channel: molecular basis of K+ conduction and selectivity. *Science* **280**, 69-77 (1998).
26. M. Hirschi *et al.*, Cryo-electron microscopy structure of the lysosomal calcium-permeable channel TRPML3. *Nature* **550**, 411-414 (2017).
27. A. I. Sobolevsky, M. P. Rosconi, E. Gouaux, X-ray structure, symmetry and mechanism of an AMPA-subtype glutamate receptor. *Nature* **462**, 745-756 (2009).
28. E. C. Twomey, M. V. Yelshanskaya, R. A. Grassucci, J. Frank, A. I. Sobolevsky, Channel opening and gating mechanism in AMPA-subtype glutamate receptors. *Nature* **549**, 60-65 (2017).

29. E. C. Twomey, A. I. Sobolevsky, Structural Mechanisms of Gating in Ionotropic Glutamate Receptors. *Biochemistry* **57**, 267-276 (2018).
30. O. S. Smart, J. G. Neduvelil, X. Wang, B. A. Wallace, M. S. Sansom, HOLE: a program for the analysis of the pore dimensions of ion channel structural models. *J Mol Graph* **14**, 354-360, 376 (1996).
31. M. G. Claros, P. Vincens, Computational Method to Predict Mitochondrially Imported Proteins and their Targeting Sequences. *European Journal of Biochemistry* **241**, 779-786 (1996).
32. I. G. Denisov, Y. V. Grinkova, A. A. Lazarides, S. G. Sligar, Directed Self-Assembly of Monodisperse Phospholipid Bilayer Nanodiscs with Controlled Size. *Journal of the American Chemical Society* **126**, 3477-3487 (2004).
33. J. Dubochet *et al.*, Cryo-electron microscopy of vitrified specimens. *Q Rev Biophys* **21**, 129-228 (1988).
34. C. Suloway *et al.*, Automated molecular microscopy: the new Leginon system. *J Struct Biol* **151**, 41-60 (2005).
35. G. C. Lander *et al.*, Appion: an integrated, database-driven pipeline to facilitate EM image processing. *J Struct Biol* **166**, 95-102 (2009).
36. A. Rohou, N. Grigorieff, CTFFIND4: Fast and accurate defocus estimation from electron micrographs. *J Struct Biol* **192**, 216-221 (2015).
37. N. R. Voss, C. K. Yoshioka, M. Radermacher, C. S. Potter, B. Carragher, DoG Picker and TiltPicker: software tools to facilitate particle selection in single particle electron microscopy. *J Struct Biol* **166**, 205-213 (2009).
38. T. Ogura, K. Iwasaki, C. Sato, Topology representing network enables highly accurate classification of protein images taken by cryo electron-microscope without masking. *J Struct Biol* **143**, 185-200 (2003).
39. M. A. Herzik, Jr., M. Wu, G. C. Lander, Achieving better-than-3-A resolution by single-particle cryo-EM at 200 keV. *Nat Methods* **14**, 1075-1078 (2017).
40. S. Q. Zheng *et al.*, MotionCor2: anisotropic correction of beam-induced motion for improved cryo-electron microscopy. *Nat Methods* **14**, 331-332 (2017).
41. D. Kimanius, B. O. Forsberg, S. H. Scheres, E. Lindahl, Accelerated cryo-EM structure determination with parallelisation using GPUs in RELION-2. *Elife* **5**, (2016).
42. A. Punjani, J. L. Rubinstein, D. J. Fleet, M. A. Brubaker, cryoSPARC: algorithms for rapid unsupervised cryo-EM structure determination. *Nature Methods* **14**, 290 (2017).
43. S. H. Scheres, S. Chen, Prevention of overfitting in cryo-EM structure determination. *Nat Methods* **9**, 853-854 (2012).
44. P. Emsley, K. Cowtan, Coot: model-building tools for molecular graphics. *Acta Crystallogr D Biol Crystallogr* **60**, 2126-2132 (2004).
45. N. W. Moriarty, R. W. Grosse-Kunstleve, P. D. Adams, electronic Ligand Builder and Optimization Workbench (eLBOW): a tool for ligand coordinate and restraint generation. *Acta Crystallogr D Biol Crystallogr* **65**, 1074-1080 (2009).
46. P. D. Adams *et al.*, PHENIX: a comprehensive Python-based system for macromolecular structure solution. *Acta Crystallogr D Biol Crystallogr* **66**, 213-221 (2010).
47. V. B. Chen *et al.*, MolProbity: all-atom structure validation for macromolecular crystallography. *Acta Crystallogr D Biol Crystallogr* **66**, 12-21 (2010).
48. F. A. Ran *et al.*, Genome engineering using the CRISPR-Cas9 system. *Nature Protocols* **8**, 2281 (2013).
49. J. B. Heymann, D. M. Belnap, Bsoft: image processing and molecular modeling for electron microscopy. *J Struct Biol* **157**, 3-18 (2007).